Dual-Barrel Conductance Micropipet as a New Approach to the Study of Ionic Crystal Dissolution Kinetics

Sophie L. Kinnear[1], *Kim McKelvey*[1,2], *Michael E. Snowden*[1], *Massimo Peruffo*[1], *Alex W. Colburn*[1] *and Patrick R. Unwin*[1]*

[1]Department of Chemistry and [2]MOAC Doctoral Training Centre, University of Warwick, Gibbet Hill Road, Coventry, CV4 7AL

*Email: p.r.unwin@warwick.ac.uk

Abstract

A new approach to the study of ionic crystal dissolution kinetics is described, based on the use of a dual-barrel theta conductance micropipet. The solution in the pipet is undersaturated with respect to the crystal of interest, and when the meniscus at the end of the micropipet makes contact with a selected region of the crystal surface, dissolution occurs causing the solution composition to change. This is observed, with better than 1 ms time resolution, as a change in the ion conductance current, measured across a potential bias between an electrode in each barrel of the pipet. Key attributes of this new technique are: (i) dissolution can be targeted at a single crystal surface; (ii) multiple measurements can be made quickly and easily by moving the pipet to a new location on the surface; (iii) materials with a wide range of kinetics and solubilities are open to study because the duration of dissolution is controlled by the meniscus contact time; (iv) fast kinetics are readily amenable to study because of the intrinsically high mass transport rates within tapered micropipets; (v) the experimental geometry is well defined, permitting finite element method modeling to allow quantitative analysis of experimental data. Herein, we study the dissolution of NaCl as an example system, with dissolution induced for just a few milliseconds, and estimate a first-order heterogeneous rate constant of 7.5 (± 2.5) $x10^{-5}$ cm s^{-1} (equivalent surface dissolution flux *ca*. 0.5 μmol cm^{-2} s^{-1} into a completely undersaturated solution). Ionic crystals form a huge class of materials whose dissolution properties are of considerable interest, and we thus anticipate that this new localized micro-scale surface approach will have considerable applicability in the future.

Introduction

Crystal dissolution processes are of ubiquitous importance across many areas of natural science,[1-3] playing a key role in many practical applications, such as in oral drug delivery[4, 5] and in a diverse range of industries from food[6] to construction.[7] Consequently, methods for studying crystal dissolution are hugely valuable, and considerable attention has been given to the development of techniques that can provide quantitive information on the kinetics and mechanisms.[8]

Crystal dissolution rates typically depend on the degree of undersaturation at the crystal/liquid interface,[9] and this is broadly governed by two competing processes in series: (i) surface phenomena, such as surface diffusion and the detachment of ions or molecules at the crystal surface; and (ii) mass transport of material from the interfacial region to the bulk solution. Clearly, mass transport must be sufficiently high and well-defined to enable the kinetics of the surface processes to be measured. Additionally, because different surfaces of a crystal, and particular sites on a surface, may have very different dissolution characteristics[10] the most informative studies are those that target well-defined and characterizable surfaces.

The need for both well-defined mass transport and well-defined surfaces has been addressed to some extent by hydrodynamic methods, including the rotating disc[11] and channel flow cell.[12, 13] These techniques deliver well-defined mass transport rates to the crystal surface and so enable intrinsic surface rates to be determined. While the rotating disc method typically follows dissolution reactions by monitoring the chemical composition of the bulk solution, the channel flow cell system allows real time electrochemical monitoring of the dissolution rate via an electrode positioned downstream of the crystal.[12] The composition of the effluent from flow cells can also be analyzed with a range of quantitative analytical techniques. [14, 15]

The primary limitation of these hydrodynamic systems is that, typically, they require crystalline material in the form of large flat surfaces, or samples embedded in a support material, and the measured dissolution rate is averaged over large areas of the surface, which potentially hides local intrinsic rate differences.[8]

A different approach to dissolution and growth measurements involves the use of scanning probe microscopy techniques, for example, *in-situ* atomic force microscopy (AFM),[16-20] and scanning electrochemical microscopy (SECM).[10] While *in-situ* AFM has provided major insights into dissolution processes there are some practical drawbacks. For instance, the process must be slower than the speed of the AFM scan and the probe may perturb the hydrodynamics and diffusion in AFM flow cells[21,] making the description of mass transport rather difficult. In general, there are often significant differences between dissolution rates measured via AFM and other techniques for the same material and conditions,[21, 22] an issue which requires further attention.

SECM studies employ an ultramicroelectrode positioned close to the surface of a crystal to induce dissolution and probe the associated fluxes.[8, 10, 23] Advantages of this approach, which has also been implemented in a combined SECM-AFM format,[24] are that dissolution is targeted at specific regions of a crystal surface and the dissolution time can be controlled very precisely (millisecond time resolution) by the electrode.[10, 23, 25] In addition, one can also study materials with a very wide range of solubilities.[25, 10] However, SECM-related methods have, hitherto, largely been limited to dissolution processes that can be triggered by the oxidation/reduction of the constituents ions or molecules of the crystal. Potentiometric electrodes have also been employed in an SECM format to measure dissolution fluxes, although without quantitative analysis,[26] and with a dual-channel nanoscale SECM-scanning ion conductance microscopy (SICM) probe to permit the high level quantitative analysis of experimental topographical and chemical images.[27]

Herein, we introduce a dual-barrel theta micropipet for rapid, multiple point conductance measurements of dissolution kinetics across a crystal surface, via meniscus contact. In other applications, dual-barrel micropipet techniques have demonstrated high spatial resolution,[28, 29] the possibility of measuring fast electrochemical kinetics on electrode surfaces,[30] and the ability to 'draw' patterns on surfaces.[29, 31] The meniscus at the end of the pipet creates a well-defined micro-conductance cell on a substrate, [28, 29, 32] without the pipet, itself, touching the surface. In general, dual pipet techniques greatly enhance the scope and information content of meniscus contact techniques for deposition[28, 29, 31]and dissolution processes,[28] compared to single pipet-based meniscus contact methods.[33-36]

We demonstrate the capabilities of the technique by studying the dissolution of the ionic crystal NaCl in aqueous solution as a model system. This system is fundamentally interesting as it is characterized by high solubility (6.1 M)[38] and relatively large dissolution fluxes which makes studies with techniques that require immersion of the solid in a bulk solvent somewhat challenging.[39] NaCl dissolution is also of practical importance in relation to developing anti-caking technologies in the food industry.[6,40, 41] Since conductance measurements[42] have been widely used for dissolution studies on a macro-scale in suspensions, we envisage that the dual-barreled conductance micropipet described herein could be widely adopted for the study of dissolution (and growth) processes. More generally, the work in this paper further enhances a growing family of quantitative pipet-based imagining techniques.[43-50]

Experimental Section

Materials. All solutions were prepared using Milli-Q water (Millipore Corp.) with a resistivity of ca.18.2 MΩ cm at 298 K. SiO_2 substrates were cut from Si/SiO_2 wafers (IDB Technologies) and were cleaned by plasma ashing (K1050X, Emitech) immediately prior to

use. The NaCl crystals were formed by evaporation in air of a droplet (~100 µl) of saturated NaCl solution (6.1 M)[38] deposited on a glass slide (Menzel-Gläser, Thermo Scientific). The crystals grew with a cubic morphology with the (100) faces exposed.[51] The crystal edge length was typically 300-500 µm.

Pipet Fabrication. Dual-barrel conductance micropipets were fabricated from borosilicate theta pipets (30-0114, Harvard Apparatus) pulled to a sharp point using a laser puller (P-2000, Sutter Instruments, pulling parameters: Heat 550, Fil 4, Vel 30, Del 120, Pul 28). Each channel of the pipet was filled with 5 mM aqueous NaCl, together with a chloridized 0.25 mm diameter silver wire (99%, MaTecK) that acted as a quasi reference counter electrode (QRCE) to form the conductance cell.[32] Experiments were performed with pipets of dimension (effective radii) r_p = 0.65 µm perpendicular to the septum, and dimension r_t = 0.4 µm parallel to the septum from the center to the inner edge (see Figure 1(a)). The pipet semi-angle (θ), as shown in the inset to Figure 1(a), was typically 8°. The tip dimensions were measured accurately with field emission-scanning electron microscopy (FE-SEM) (Supra 55-VP, Zeiss). The outside walls of the pipet were silanized with dimethyldichlorosilane which functionalized the glass with a hydrophobic coating thereby keeping the meniscus confined to the end of the pipet.[32]

Instrumentation. The experimental setup was similar to that reported previously for scanning electrochemical cell microscopy (SECCM) studies.[30] As Figure 1(b) shows, the sample was mounted on an *xy* piezoelectric positioning stage (Nano-Bio300, MadCityLabs). A camera (T110604, PixeLink) was angled such that the tip could be seen easily. The vertical position of the pipet was controlled by a separate *z* piezoelectric positioner (P-753.3CD, Physik Instrumente). The ion current between the QRCEs was recorded using a high sensitivity current/voltage converter (constructed in house) typically at a sensitivity of

10 nA/V. The system was controlled though a field programmable gate array (FPGA) card (PCI-7830R, National Instruments) by a PC running Labview (11.0, National Instruments) software written in-house. Data were typically recorded at 25.2 kHz. The instrumentation was operated in an air-conditioned laboratory at a temperature of 22 ± 1 °C.

Analytical methodology. The current measured between the two QRCEs depends on the voltage applied between the QRCEs, which was 0.4 V and overall resistance of the theta pipet cell. While in air, a small meniscus is formed at the tip of the pipet (see schematic in Figure 1(c)(i)), resulting in a high resistance, and consequently only a small current is detected (*vide infra*).[28] The experimental procedure was to approach the pipet towards the surface at a speed of 0.1 μm s^{-1} until the meniscus at the end of the pipet wetted the substrate surface, without the pipet itself making contact. This phenomenon was readily detected, because when the meniscus wets the surface its thickness increases, resulting in the meniscus resistance decreasing, as manifested by a sharp increase in the ion conductance current (Figure 1(c)(ii)). The abrupt change in conductance current (due to a 'jump to contact' of the meniscus with the surface)[32] was sensed and used to automatically stop the motion of the pipet, which was then held in a fixed position for a predefined etch time (*vide infra*). Dissolution was promoted by the use of a greatly undersaturated solution in the pipet with respect to sodium chloride. The resulting ionic dissolution flux from the crystal surface into the solution in the meniscus and pipet further decreased the resistance between the two QRCEs and hence increased the current on a longer timescale. In fact, as we show below, the barrel current-time response is related to the flux of ions from the crystal surface. Once the pre-defined dissolution time had elapsed, the tip was withdrawn at a speed of 100 μm s^{-1} to ensure that contact between the meniscus and substrate was broken abruptly (Figure 1(c)(iii)).

Repeat measurements were performed by laterally repositioning (typically by 5 μm) the tip over a new section of the micro-crystal surface. Figure 1(d) shows an image taken *in-situ*

during a typical experiment using a camera in which the pipet and a series of dissolution pits can be seen. The pits formed using this procedure were characterized by optical microscopy (BH-2, Olympus), as shown in the inset of Figure 1(d), and AFM (Veeco BioScope Catalyst Atomic Force Microscope, Bruker) in "Scan Asyst" mode with a Nanoscope V controller (Veeco), using Sb doped Si tips (SNL-10, Veeco).

Finite Element Method Modeling. The commercial finite element method (FEM) simulation package Comsol Multiphysics (v4.3, Comsol AB) with LiveLink for Matlab (R2011a, Mathworks) was used for all simulations. Simulations were performed using a 3D geometric domain of the meniscus and tip of the pipet, similar to that described previously,[32] and shown in Figure 2.

The variation of the ionic conductance current with respect to time, due to the dissolution process, was calculated in 2 stages. In stage 1, the time-dependent Na^+ and Cl^- concentrations were determined from a diffusion-only simulation. In stage 2, the corresponding steady-state electric field at each time step was determined and from this the conductance current between the barrels, i_b, was calculated.

The diffusion-only mass transport of Na^+ and Cl^- was reasonable for the experimental conditions of interest because the applied bias was relatively small.[32] Moreover, we focus on short time measurements (< 15 ms) where concentration gradients are relatively in the region of interest (vicinity of the meniscus and pipet tip), and the impact of the electric field in this region is rapidly diminished by the flood of ions from the crystal surface due to dissolution. Focusing on the short time behavior also allowed us to reasonably assume a static surface, although moving boundaries could be incorporated in the future, as we have shown for recent micro-scale dissolution studies by other methods.[23,]

The time-dependent concentration profiles, within the pipet tip, are determined by solving Fick's second law:

$$\frac{dc}{dt} = D\nabla^2 c \qquad (1)$$

where t, c, and D are the time, concentration and diffusion coefficient, respectively. Because dissolution is stoichiometric and the solution has to be electroneutral, we considered a one species problem, with the mean diffusion coefficient of Na^+ and Cl^- (16.83×10^{-6} cm^2 s^{-1}).[52]

The upper faces of the pipet barrels (boundaries 1 and 2 in Figure 2(b)), representing bulk solution, were defined by,

$$c = c^* \qquad (2)$$

where c^* was the starting concentration of the NaCl solution (5 mM). The rate of dissolution at the substrate surface (boundary 5) was assumed to be first-order with respect to the degree of undersaturation at the crystal solution interface,

$$\mathbf{n}.\mathbf{N} = k(c_{sat} - c) \qquad (3)$$

where **n** is the inward unit vector normal to the surface, **N** is the flux vector, k is a first-order dissolution rate constant (cm s^{-1}) and c_{sat} was the saturation concentration (6.1 M).[38] In fact, as shown herein, c_{sat} is extremely large compared to c near the interface, so that we essentially measure the flux as kc_{sat}. The pipet walls (boundary 3 in Figure 2(b)) and the meniscus/air interface (boundary 4) were considered to have no flux.

Concentration profiles were output every 0.1 ms from t = 0 s to t = 15 ms, and each concentration profile was subsequently used as a basis to calculate the electric field, and therefore the corresponding conductance current in stage 2.

The potential field within the pipet and meniscus was determined at each time step by solving the governing equation for a steady-state electric field:

$$\mathbf{J} = \sigma \nabla V \qquad (4)$$

where **J** is the current density vector, σ is the conductivity and V is the potential, while ensuring the conservation of current within the simulation domain:

$$\nabla \mathbf{J} = 0 \qquad (5)$$

The conductivity of the solution within the pipet and meniscus was determined from:[53]

$$\sigma = (z_{Na^+}^2 u_{Na^+} c + z_{Cl^-}^2 u_{Cl^-} c) \qquad (6)$$

where z_i is the charge and u_i is the ionic conductivity of species i, (u_{Na+} = 76.31 S cm^2 mol^{-1} and u_{Cl-} = 50.08 S cm^2 mol^{-1}). The conductance current (i_b) can be calculated from the current density vector (**J)** by taking the surface integral across a cross-section of one of the barrels.

For the electric field calculations, the upper faces of the pipet barrels (boundaries 1 and 2 in Figure 2(b)) have an applied bias between them, mimicking the experimental conditions.

Results and Discussion

Ion Conductance Measurements. The localized dissolution of NaCl crystals was carried out using a pipet, with dimensions defined in Figure 1(a), containing NaCl solution (5 mM). A typical experimental conductance current-time trace is shown in Figure 3(a), with the corresponding pipet position below, shown schematically, with respect to the crystal surface. Figure 3(b) shows traces for 4 dissolution times of 3, 10, 15 and 18 ms. For each meniscus contact time there are multiple overlaid current-time traces (between 2 and 12 runs for each

etch time) and each trace was recorded in a separate region of the surface. These data serve to highlight the high reproducibility of meniscus landing and localized crystal dissolution. It should be noted that between dissolution experiments the current decays back to the original value.

When the pipet was in air, $t < 0$, the conductance current, i_b, had a low value *ca.* 0.1 nA, because the meniscus at the end of the pipet was rather thin, causing high resistance.[32] During this period the pipet was moving towards the surface at a speed of 0.1 μm s^{-1} as illustrated in Figure 3(a)(i). The liquid meniscus contact with the NaCl surface at $t = 0$ is observed as a jump to contact wetting of the surface causing the current to abruptly increase by about an order of magnitude. This is due to the decreased resistance from the larger meniscus as illustrated in Figure 3(a)(ii), and manifested in the conductance current-time traces at $t = 0$ in Figure 3(b). This phenomenon has been documented for other systems studied by the related SECCM technique.[28,32,] The increase in current was detected by the control program and used to stop the pipet approach, leaving the meniscus stationary on the surface, as illustrated by the constant height of the vertical position of the pipet, shown in Figure 3(a)(ii). After the initial current jump there was a gradual increase in the conductance current with time, attributed to the release of ions from the NaCl crystal into the meniscus. After a predefined time, the pipet was moved away from the NaCl surface at a speed of 100 μm s^{-1}, which broke the meniscus contact with the crystal and caused the current to fall rapidly as the meniscus shrank in size when detached from the surface (Figure 3(a)(iii)). As explained above, there was a large degree of reproducibility in the currents recorded in different spots of the crystal, as the curves for a particular time overlap to a high degree. In addition the traces at different times overlap up until the point at which meniscus contact with the crystal surface was broken (Figure 3(b)).

Before these current-time traces were analyzed, the current response associated with initial contact of the meniscus with the surface, and the establishment of a stable meniscus contact was assessed. This was done by comparing the response for meniscus contact to a NaCl crystal to that for an inert SiO_2 surface, as shown in Figure 4. On SiO_2 the rise time (defined as the time for the current to change from 10% to 90% of the maximum current signal) was 0.3 ms. This time is an order of magnitude longer than the rise time of the current follower used for the measurement and so this rise time was essentially associated with the meniscus stabilizing on the surface. This meniscus stabilization time is also at least an order of magnitude shorter than the dissolution periods considered.

In order to compare the conductance current of NaCl dissolution to the simulation results, it was necessary to account for the effect of meniscus stabilization. This was reasonably accomplished by subtracting the current response on SiO_2 from the response on NaCl, thereby leaving only the change in current with time that was a direct result of crystal dissolution. Both substrates are expected to have similar wettabilities by water, and we have shown that the degree of wetting of a substrate by the meniscus from a micropipet is similar on quite a wide range of substrates, because this is controlled not only by the substrate but also by the pipet outer wall, which is silanized. [28,30-32,,]

Simulations and modeling. To deduce dissolution kinetics and fluxes, we used the model outlined earlier. Typical simulated concentration maps are shown in Figure 5(a) for a pipet of dimensions: m_h = 300 nm, r_p = 0.65 μm, r_t = 0.4 μm, θ = 8°, k = 5x10^{-5} cm s^{-1} and m_c = 3.2 μm. The latter was determined from measurement of dissolution pit dimensions by AFM (see below) and represents a reasonable upper limit on the effective contact area of the meniscus with the crystal surface. The corresponding electric field maps are shown in Supporting Information, Figure S1. At t = 0 s the pipet is filled homogenously with bulk solution (5 mM). At t = 5 ms (Figure 5(a)) the dissolution of NaCl leads to an appreciable

increase of the concentration of Na^+ and Cl^- ions in the meniscus and the mouth of the pipet, leading to an increase in conductance current (*vide supra*) and corresponding smaller electric field gradient in this region of the pipet (Supporting Information, Figure S1). At t = 10 ms further dissolution has occurred, with ions pumped into the meniscus and transported into the pipet. The concentration profile of Na^+ and Cl^- ions extends further up the pipet as time increases which results in a further increase in the conductance current and concomitant change in the electric field (Supporting Information Figure S1). However, even for the longest dissolution time considered, the concentration in the meniscus near the crystal surface reaches a maximum of <1% of the saturated value, highlighting that, with these parameters, typically representative of experiments, the dissolution process is essentially under surface kinetic control.

The simulations were run for a wide range of dissolution rate constants; see Figure 5(b). As the dissolution rate constant increases, the magnitude of the conductance current - as a function of time, increases. It can be seen that the technique is sensitive to a wide range of dissolution rate constants with values of k up to *ca.* 0.1 cm s^{-1} reasonably accessible, above which it is difficult to distinguish the surface rate constants from the mass transport limit. The relatively high rate constant amenable to characterization is a consequence of the intrinsically high mass transport rates inherent in the tapered micropipette design.[32, 45]

Figure 5(b) shows background subtracted experimental current-time curves for 2 runs along with a range of simulated currents for different dissolution rates. The experimental data were typical of more than 20 traces run (see Figure 3(b)). There was reasonably good agreement between the experimental data and the simulated data with a fit to $k = 5 \times 10^{-5}$ cm s^{-1} for longer times and $k = 1 \times 10^{-4}$ cm s^{-1} at t < 3 ms. We thus assign a value of intrinsic dissolution rate of 7.5 (± 2.5) x 10^{-5} cm s^{-1} and an intrinsic surface-controlled dissolution flux (kc_{sat}) of *ca*. 0.5 µmol cm^{-2} s^{-1}. The kinetic constant and flux is of the same order as found in a previous study

(~10^{-5} cm s^{-1}) for compacted disk samples[54] confirming the validity of the technique. Other ionic crystals have a wide range of dissolution rates, including KF which has a reported rate constant of ~$3x10^{-8}$ cm s^{-1} [37] and CaSO3 which, in its common form of gypsum, has a dissolution rate of ~$6x10^{-4}$ cm s^{-1}.[14]

We assumed a meniscus height of 300 nm, as deduced from a control measurement on SiO_2 and guided by previous related SECCM studies.[28-32] However, we investigated the impact of the meniscus height on the current response through further simulations, and found it to be negligible over a reasonable range of values, as shown in the supporting information (Figure S3). This meniscus height insensitivity arises from the fact that the concentration gradient of Na^+ and Cl^- extends up into the barrels, (see Figure 5(a)) resulting in the meniscus height from the surface representing only a small percentage of the overall distance of the diffusion profile. This demonstrates that the important geometric parameters in the model are the footprint of the meniscus on the surface, the size and shape of which are easily determined from SEM. The meniscus contact area was determined from the AFM of the dissolution pits (below), but given some redistribution of material in the droplet left on the surface, this represents an upper limit for the meniscus contact area, and thus a lower limit on the intrinsic dissolution rate.

Dissolution Pit Morphology Measurements. AFM measurements were performed prior to and after dissolution experiments to characterize the crystal surface, and the size and shape of pits formed by dissolution. AFM images were analyzed using SPIP 6.0.10 (Image Metrology). Prior to dissolution, the NaCl crystals showed no major features and had a surface roughness of ~10 nm. After dissolution, pit features were clearly visible, and AFM was used to measure the morphology and dimensions. Figure 6 shows an AFM image of 9 typical pits, each produced with a dissolution time of 10 (±0.2) ms. Dissolution pits were circular and had an average diameter of 3.2 (±0.1) µm at 10 ms. The diameter did not change

significantly with dissolution time, with a diameter of 3.1 (±0.05 μm) at 3 ms and 3.3 (±0.1) at 15 ms. Furthermore, the depths of the pits showed a relatively minor dependence on etch time, with depths (edge to base), of 105 nm (3 ms), 131 nm (10 ms), 136 nm (15 ms). This insensitivity of the pit geometry to dissolution time suggests that the pits are a consequence of the solution left behind when the meniscus detaches, as used deliberately in some nanocrystal growth studies,[55] as discussed below.

It is interesting to compare the dissolution pit depths to the values that might be expected based on the conductance measurements. A surface-controlled dissolution flux *ca*. 0.5 μmol cm^{-2} s^{-1} suggests that the pit depths should be much smaller than seen *ca*. 0.4 nm (3 ms), 1.3 nm (10 ms), 2.0 nm (15 ms) using the known density of NaCl of 2.17 g cm^{-3} (and formula mass, 58.44 g mol^{-1}).[52] Closer inspection of the pits in Figure 6 indicates that not only has much more substantial dissolution occurred, but also that there is reprecipitation of material around the top surface of the pit. A reasonable explanation for this morphology and the much deeper pits than expected is that solution is retained on the locally dissolving crystal surface as meniscus contact is broken and dissolution continues in the highly undersaturated solution (*vide supra*) along with evaporation of the droplet. For the present study this is advantageous as it marks the likely (maximum) surface area covered by the droplet. There may be some lateral dissolution of the surface by the retained droplet, but the extent of this would be of the order of the final pit depth (*ca.* 100 nm, *vide supra*) and so is essentially negligible compared to the estimated wetting area. It is important to note that the dissolution by a small retained volume of solution is exacerbated for this particular system because the solution in the meniscus is highly undersaturated with respect to the highly soluble NaCl. For less soluble materials characterized by fast kinetics such effects would be negligible, and it would be possible to elucidate dissolution kinetics by the measurement of pit depths and/or conductance currents.

Conclusions

We have presented the first use of a dual-barrel conductance micropipet as a new method for studying ionic crystal dissolution kinetics. Multiple conductance measurements across a crystal surface produce highly reproducible current-time measurements with high temporal resolution that are sensitive to the rate of dissolution of the surface.

A key feature of the technique is that the sample is only exposed to the solution where the meniscus makes contact, and that measurements can be made with sub-millisecond time resolution, opening up the possibility of studying materials with a wide range of solubilities and particularly highly soluble crystals. The study of the NaCl crystals provided a first-order rate constant for dissolution of 7.5 (± 2.5) $x10^{-5}$ cm s^{-1} (or equivalent intrinsic dissolution flux *ca*. 0.5 μmol cm^{-2} s^{-1}) determined by comparing FEM simulations to experimental conductance current data. These values are in good agreement with earlier measurements, serving to validate the technique.[34-38,47] A further strength of the technique is that it is amenable to a high level quantitative description of mass transport and surface kinetics. Simulations demonstrate dissolution kinetics with rate constants, *k*, up to *ca*. 0.1 cm s^{-1}, assuming a first order process in interfacial undersaturation, which is larger than any reported ionic crystal dissolution rate should be measureable. The simulation could, if required, incorporate more complex dissolution kinetics and so be applicable to a wide range of materials.

In the future, it should be possible to use the micropipet (or even a nanopipet) to scan over a surface, providing an opportunity to study the impact of surface heterogeneities on dissolution kinetics at a quantitative level with high spatial resolution.[28] Moreover, there should also be scope for determining kinetics through the analysis of the local etch features

produced. This was not possible in the present study of NaCl due owing to its very high solubility, and relatively low rate constant, leading to the continued dissolution and reprecipitation of material by a small amount of solution retained on the crystal surface.

Associated Content

Supporting Information. Additional data from the FEM simulations. This material is available free of charge via the Internet at http://pubs.acs.org.

Acknowledgements

We thank the European Research Council for providing funding for S.L.K, M.E.S, M.P, K.M and P.R.U. though the European Community's (EC's) Seventh Framework Programme (FP7/2007-2013)/ERC-2009-AdG2471143-QUANTIF and the EPSRC for a MOAC/DTC studentship for K.M. We also acknowledge the support of Advantage West Midlands Science City Advanced Materials Project and the European Regional Development Fund for providing some of the equipment used in this work.

References

1. Zhang, L.; Lüttge, A., Theoretical approach to evaluating plagioclase dissolution mechanisms. *Geochimica et Cosmochimica Acta* **2009,** *73* (10), 2832-2849.
2. Wang, S.-S.; Xu, A.-W., Amorphous Calcium Carbonate Stabilized by a Flexible Biomimetic Polymer Inspired by Marine Mussels. *Crystal Growth & Design* **2013,** *13* (5), 1937-1942.
3. Langer, M. R., Assessing the Contribution of Foraminiferan Protists to Global Ocean Carbonate Production. *J. Eukaryot. Microbiol.* **2008,** *55* (3), 163-169.
4. Vippagunta, S. R.; Brittain, H. G.; Grant, D. J. W., Crystalline solids. *Advanced Drug Delivery Reviews* **2001,** *48* (1), 3-26.
5. Wen, H.; Li, T.; Morris, K. R.; Park, K., Dissolution Study on Aspirin and α-Glycine Crystals. *The Journal of Physical Chemistry B* **2004,** *108* (30), 11219-11227.
6. Bode, A. A. C.; Vonk, V.; van den Bruele, F. J.; Kok, D. J.; Kerkenaar, A. M.; Mantilla, M. F.; Jiang, S.; Meijer, J. A. M.; van Enckevort, W. J. P.; Vlieg, E., Anticaking Activity of Ferrocyanide on Sodium Chloride Explained by Charge Mismatch. *Crystal Growth & Design* **2012,** *12* (4), 1919–1924.
7. Charola, E.; Pühringer, J.; Steiger, M., Gypsum: a Review of its Role in the Deterioration of Building Materials. *Environmental Geology* **2006,** *52* (2), 339-352.
8. Unwin, P. R.; Macpherson, J. V., New Strategies for Probing Crystal Dissolution Kinetics at the Microscopic Level. *Chemical Society Reviews* **1995,** *24* (2), 109-119.
9. Dejmek, M.; Ward, C. A., A Statistical Rate Theory Study of Interface Concentration during Crystal Growth or Dissolution. *The Journal of Chemical Physics* **1998,** *108* (20), 8698-8704.
10. Macpherson, J. V.; Unwin, P. R., Scanning Electrochemical Microscopy as a Probe of Silver Chloride Dissolution Kinetics in Aqueous Solutions. *The Journal of Physical Chemistry* **1995,** *99* (40), 14824-14831.
11. Sjoeberg, E. L.; Rickard, D. T., Calcite Dissolution Kinetics: Surface Speciation and the Origin of the Variable pH Dependence. *Chem. Geol.* **1984,** *42*, 119-136.
12. Orton, R.; Unwin, P. R., Dolomite Dissolution Kinetics at Low pH: a Channel-Flow Study. *Journal of the Chemical Society, Faraday Transactions* **1993,** *89* (21), 3947-3954.
13. Peltonen, L.; Liljeroth, P.; Heikkilä, T.; Kontturi, K.; Hirvonen, J., Dissolution testing of acetylsalicylic acid by a channel flow method—correlation to USP basket and intrinsic dissolution methods. *European Journal of Pharmaceutical Sciences* **2003,** *19* (5), 395-401.
14. Mbogoro, M. M.; Snowden, M. E.; Edwards, M. A.; Peruffo, M.; Unwin, P. R., Intrinsic Kinetics of Gypsum and Calcium Sulfate Anhydrite Dissolution: Surface Selective Studies under Hydrodynamic Control and the Effect of Additives. *The Journal of Physical Chemistry C* **2011,** *115* (20), 10147-10154.
15. Lehto, P.; Aaltonen, J.; Niemelä, P.; Rantanen, J.; Hirvonen, J.; Tanninen, V. P.; Peltonen, L., Simultaneous Measurement of Liquid-Phase and Solid-Phase Transformation Kinetics in Rotating Disc and Channel Flow Cell Dissolution Devices. *International Journal of Pharmaceutics* **2008,** *363* (1–2), 66-72.
16. De Yoreo, J. J.; Zepeda-Ruiz, L. A.; Friddle, R. W.; Qiu, S. R.; Wasylenki, L. E.; Chernov, A. A.; Gilmer, G. H.; Dove, P. M., Rethinking Classical Crystal Growth Models through Molecular Scale Insights: Consequences of Kink-Limited Kinetics. *Cryst. Growth Des.* **2009,** *9*, 5135-5144.
17. Wu, C.; Zhao, K.; Wang, X.; Cao, M.; Xu, H.; Lu, J. R., Dissolution of the Calcite (104) Face under Specific Calcite-Aspartic Acid Interaction As Revealed by in Situ Atomic Force Microscopy. *Crystal Growth & Design* **2012,** *12* (5), 2594-2601.
18. Harstad, A. O.; Stipp, S. L. S., Calcite Dissolution: Effects of Trace Cations Naturally Present in Iceland Spar Calcites. *Geochimica et Cosmochimica Acta* **2007,** *71* (1), 56-70.
19. Guo, S.; Ward, M. D.; Wesson, J. A., Direct Visualization of Calcium Oxalate Monohydrate Crystallization and Dissolution with Atomic Force Microscopy and the Role of Polymeric Additives. *Langmuir* **2002,** *18* (11), 4284-4291.
20. Jung, T.; Sheng, X.; Choi, C. K.; Kim, W.-S.; Wesson, J. A.; Ward, M. D., Probing Crystallization of Calcium Oxalate Monohydrate and the Role of Macromolecule Additives with in Situ Atomic Force Microscopy. *Langmuir* **2004,** *20* (20), 8587-8596.

21. Gasperino, D.; Yeckel, A.; Olmsted, B. K.; Ward, M. D.; Derby, J. J., Mass Transfer Limitations at Crystallizing Interfaces in an Atomic Force Microscopy Fluid Cell: A Finite Element Analysis. *Langmuir* **2006,** *22* (15), 6578-6586.
22. Dove, P. M.; Platt, F. M., Compatible Real-Time Rates of Mineral Dissolution by Atomic Force Microscopy (AFM). *Chemical Geology* **1996,** *127* (4), 331-338.
23. McGeouch, C.-A.; Peruffo, M.; Edwards, M. A.; Bindley, L. A.; Lazenby, R. A.; Mbogoro, M. M.; McKelvey, K.; Unwin, P. R., Quantitative Localized Proton-Promoted Dissolution Kinetics of Calcite Using Scanning Electrochemical Microscopy (SECM). *The Journal of Physical Chemistry C* **2012,** *116* (28), 14892-14899.
24. Jones, C. E.; Unwin, P. R.; Macpherson, J. V., In Situ Observation of the Surface Processes Involved in Dissolution from the Cleavage Surface of Calcite in Aqueous Solution Using Combined Scanning Electrochemical–Atomic Force Microscopy (SECM-AFM). *ChemPhysChem* **2003,** *4* (2), 139-146.
25. Macpherson, J. V.; Unwin, P. R., A Novel Approach to the Study of Dissolution Kinetics using the Scanning Electrochemical Microscope: Theory and Application to Copper Sulfate Pentahydrate Dissolution in Aqueous Sulfuric Acid Solutions. *The Journal of Physical Chemistry* **1994,** *98* (6), 1704-1713.
26. Etienne, M.; Schulte, A.; Mann, S.; Jordan, G.; Dietzel, L. D.; Schuhmann, W., Constant-distance Mode Scanning Potentiometry. 1. Visualization of Calcium Carbonate Dissolution in Aqueous Solution. *Analytical Chemistry* **2004,** *76* (13), 3682-3688.
27. Nadappuram, B. P.; McKelvey, K.; Al Botros, R.; Colburn, A. W.; Unwin, P. R., Fabrication and Characterization of Dual Function Nanoscale pH-Scanning Ion Conductance Microscopy (SICM) Probes for High Resolution pH Mapping. *Analytical Chemistry* **2013**.
28. Ebejer, N.; Schnippering, M.; Colburn, A. W.; Edwards, M. A.; Unwin, P. R., Localized High Resolution Electrochemistry and Multifunctional Imaging: Scanning Electrochemical Cell Microscopy. *Analytical Chemistry* **2010,** *82* (22), 9141-9145.
29. Rodolfa, K. T.; Bruckbauer, A.; Zhou, D.; Korchev, Y. E.; Klenerman, D., Two-Component Graded Deposition of Biomolecules with a Double-Barreled Nanopipette. *Angewandte Chemie International Edition* **2005,** *44* (42), 6854-6859.
30. Lai, S. C. S.; Patel, A. N.; McKelvey, K.; Unwin, P. R., Definitive Evidence for Fast Electron Transfer at Pristine Basal Plane Graphite from High-Resolution Electrochemical Imaging. *Angewandte Chemie International Edition* **2012,** *51* (22), 5260-5260.
31. McKelvey, K.; O'Connell, M. A.; Unwin, P. R., Meniscus Confined Fabrication of Multidimensional Conducting Polymer Nanostructures with Scanning Electrochemical Cell Microscopy (SECCM). *Chemical Communications* **2013,** *49* (29), 2986-2988.
32. Snowden, M. E.; Gueell, A. G.; Lai, S. C. S.; McKelvey, K.; Ebejer, N.; O'Connell, M. A.; Colburn, A. W.; Unwin, P. R., Scanning Electrochemical Cell Microscopy: Theory and Experiment for Quantitative High Resolution Spatially-Resolved Voltammetry and Simultaneous Ion-Conductance Measurements. *Analytical Chemistry* **2012,** *84* (5), 2483-2491.
33. Zhan, D.; Yang, D.; Zhu, Y.; Wu, X.; Tian, Z.-Q., Fabrication and characterization of nanostructured ZnO thin film microdevices by scanning electrochemical cell microscopy. *Chemical Communications* **2012,** *48* (93), 11449-11451.
34. Laslau, C.; Williams, D. E.; Kannan, B.; Travas-Sejdic, J., Scanned Pipette Techniques for the Highly Localized Electrochemical Fabrication and Characterization of Conducting Polymer Thin Films, Microspots, Microribbons, and Nanowires. *Advanced Functional Materials* **2011,** *21* (24), 4607-4616.
35. Hu, J.; Yu, M.-F., Meniscus-Confined Three-Dimensional Electrodeposition for Direct Writing of Wire Bonds. *Science* **2010,** *329* (5989), 313-316.
36. Chen, C.-C.; Zhou, Y.; Baker, L. A., Scanning Ion Conductance Microscopy. *Annual Review of Analytical Chemistry* **2012,** *5* (1), 207-228.
37. Hamza, S. M.; Hamdona, S. K., Kinetics of dissolution of calcium fluoride crystals in sodium chloride solutions: influence of additives. *The Journal of Physical Chemistry* **1991,** *95* (8), 3149-3152.
38. Burgess, J., *Metal Ions in Solution*. Halsted Press: New York, 1978.

39. Wagner, C., The Dissolution Rate of Sodium Chloride with Diffusion and Natural Convection as Rate-Determining Factors. *The Journal of Physical and Colloid Chemistry* **1948,** *53* (7), 1030-1033.
40. Lipasek, R. A.; Ortiz, J. C.; Taylor, L. S.; Mauer, L. J., Effects of Anticaking Agents and Storage Conditions on the Moisture Sorption, Caking, and Flowability of Deliquescent Ingredients. *Food Research International* **2012,** *45* (1), 369–380.
41. Bode, A. A. C.; Jiang, S.; Meijer, J. A. M.; van Enckevort, W. J. P.; Vlieg, E., Growth Inhibition of Sodium Chloride Crystals by Anticaking Agents: In Situ Observation of Step Pinning. *Crystal Growth & Design* **2012,** *12* (12), 5889-5896.
42. Tomson, M. B.; Nancollas, G. H., Mineralization Kinetics: A Constant Composition Approach. *Science* **1978,** *200*, 1059-1060.
43. Hansma, P.; Drake, B.; Marti, O.; Gould, S.; Prater, C., The scanning ion-conductance microscope. *Science* **1989,** *243* (4891), 641-643.
44. Rheinlaender, J.; Schaeffer, T. E., Image formation, resolution, and height measurement in scanning ion conductance microscopy. *Journal of Applied Physics* **2009,** *105* (9).
45. Taylor, G.; Girault, H. H. J., Ion Transfer Reactions Across a Liquid—Liquid Interface Supported on a Micropipette Tip. *Journal of Electroanalytical Chemistry and Interfacial Electrochemistry* **1986,** *208* (1), 179-183.
46. Rheinlaender, J.; Geisse, N. A.; Proksch, R.; Schäffer, T. E., Comparison of Scanning Ion Conductance Microscopy with Atomic Force Microscopy for Cell Imaging. *Langmuir* **2010,** *27* (2), 697-704.
47. Sánchez, D.; Anand, U.; Gorelik, J.; Benham, C. D.; Bountra, C.; Lab, M.; Klenerman, D.; Birch, R.; Anand, P.; Korchev, Y., Localized and non-contact mechanical stimulation of dorsal root ganglion sensory neurons using scanning ion conductance microscopy. *Journal of Neuroscience Methods* **2007,** *159* (1), 26-34.
48. Takahashi, Y.; Murakami, Y.; Nagamine, K.; Shiku, H.; Aoyagi, S.; Yasukawa, T.; Kanzaki, M.; Matsue, T., Topographic imaging of convoluted surface of live cells by scanning ion conductance microscopy in a standing approach mode. *Physical Chemistry Chemical Physics* **2010,** *12* (34), 10012-10017.
49. Chen, C.-C.; Zhou, Y.; Morris, C. A.; Hou, J.; Baker, L. A., Scanning Ion Conductance Microscopy Measurement of Paracellular Channel Conductance in Tight Junctions. *Analytical Chemistry* **2013,** *85* (7), 3621-3628.
50. Shen, M.; Ishimatsu, R.; Kim, J.; Amemiya, S., Quantitative Imaging of Ion Transport through Single Nanopores by High-Resolution Scanning Electrochemical Microscopy. *Journal of the American Chemical Society* **2012,** *134* (24), 9856-9859.
51. Pastero, L.; Aquilano, D.; Moret, M., Selective Adsorption/Absorption of Formamide in NaCl Crystals Growing from Solution. *Crystal Growth & Design* **2012,** *12* (5), 2306-2314.
52. Lide, R., *CRC Handbook of Chemistry and Physics*. CRC Press: USA, 2008.
53. Newman, J. S., *Electrochemical Systems*. Wiley: New Jersey, 2004.
54. Simon, B., Dissolution Rates of NaCl and KCl in Aqueous Solution. *Journal of Crystal Growth* **1981,** *52* (2), 789-794.
55. Stephens, C. J.; Kim, Y.-Y.; Evans, S. D.; Meldrum, F. C.; Christenson, H. K., Early Stages of Crystallization of Calcium Carbonate Revealed in Picoliter Droplets. *Journal of the American Chemical Society* **2011,** *133* (14), 5210-5213.

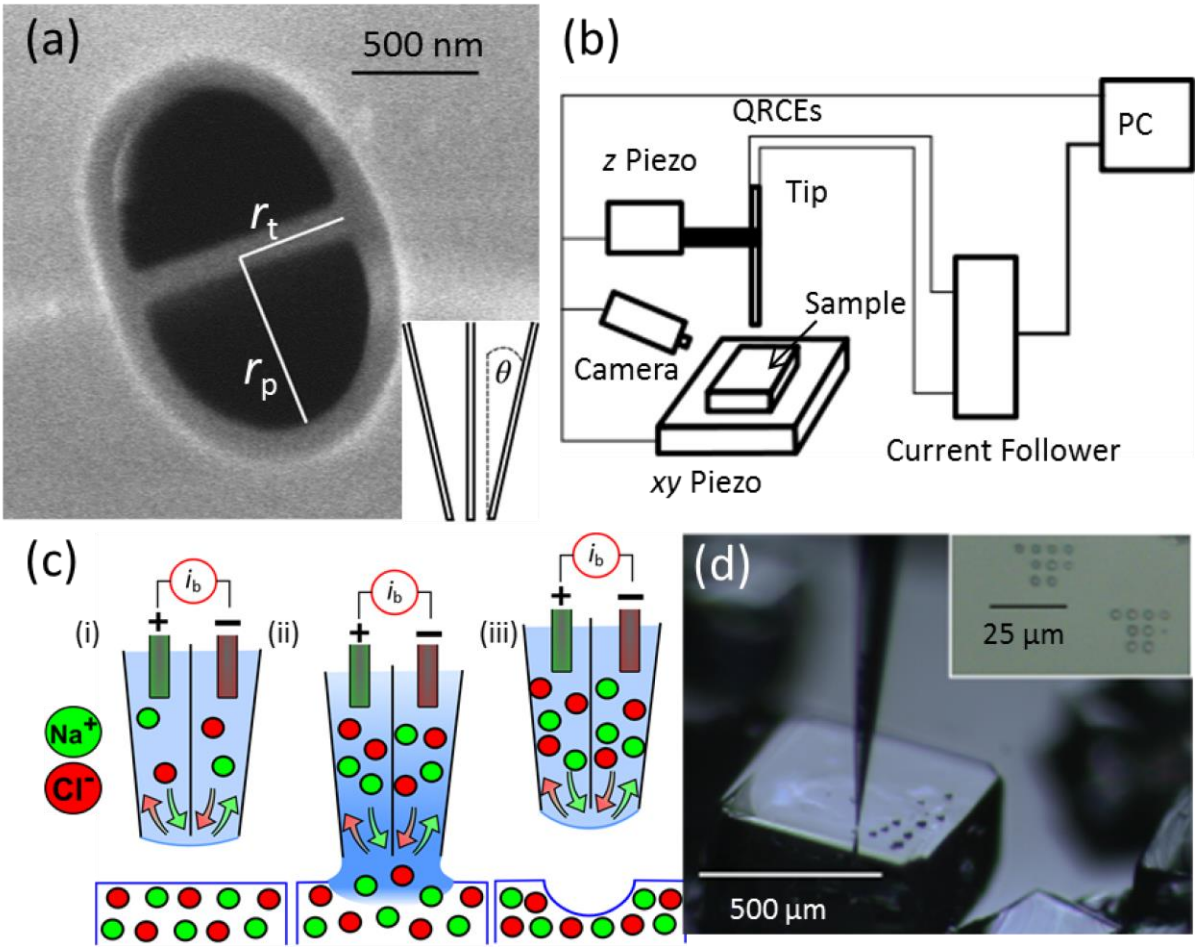

Figure 1. (a) FE-SEM image of the end of a typical pipet with the dimension perpendicular to the septum (r_p), and parallel to the septum (r_t) labeled. The inset is a sketch of the side view of a tip showing the semi-angle (θ). (b) Schematic of the experimental setup. The sample is mounted on an *xy* piezoelectric positioner, while the pipet is on a *z* piezoelectric positioner. The current is measured by a home-built current follower and all components are controlled, and data recorded, by a PC (see experimental section for details). (c) Schematic of the dissolution experimental procedure: (i) pipet held in air; (ii) dissolution occurs upon contact of the meniscus with the crystal for a defined short period; (iii) tip is retracted, breaking meniscus contact with the surface. (d) An optical microscope image taken *in-situ* from a side-mounted camera of a dual-barrel conductance micropipet aligned above a NaCl microcrystal where a series of dissolution pits can be seen. Inset: optical microscope image of two arrays of NaCl dissolution pits.

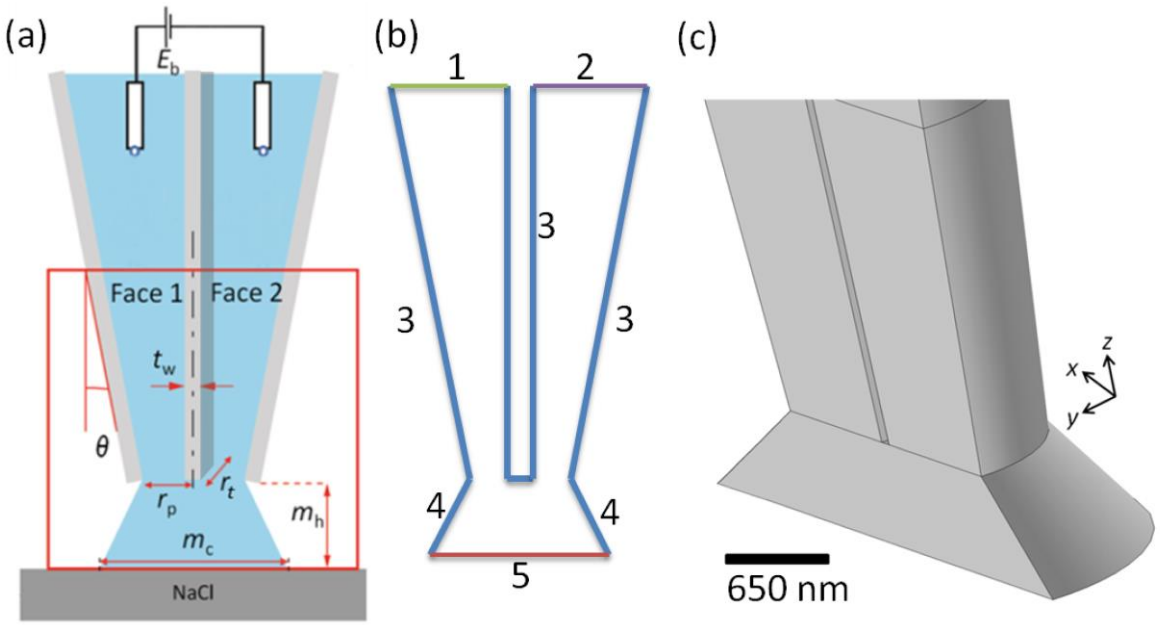

Figure 2. (a) Schematic of a pipet in contact with a NaCl crystal via a meniscus. The red box is the simulation domain with key parameters being the potential difference between the barrels (E_b), the septum width (t_w), semi-angle (θ), pipet radius (r_p), meniscus contact diameter (m_c) and meniscus height (m_h). (b) 2D sketch of the simulation domain where boundaries 1 and 2 have an applied potential imposed together with bulk concentrations, 3 and 4 are boundaries with no normal flux and 5 has a flux boundary condition, as it represents the crystal surface. (c) 3D representation of the simulation domain.

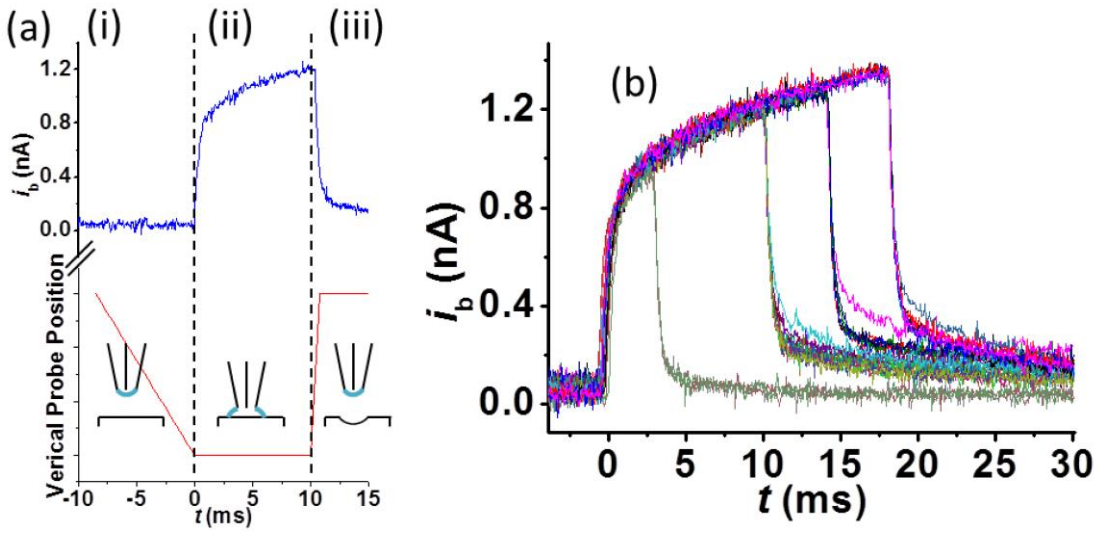

Figure 3. (a) Plot of barrel conductance current-time above a schematic of the corresponding vertical pipet position during a dissolution experiment. (i) The pipet is moving down towards the surface in air and the barrel current is small, due to a tiny meniscus. (ii) The meniscus lands as a 'jump to contact' and the pipet stops moving. The crystal dissolves causing a further increase in the barrel current. (iii) The pipet is drawn up quickly, breaking the meniscus contact and causing the current to drop as the meniscus returns to its original shape. (b) Current-time plots of multiple repeat measurements of dissolution pits at different spots on NaCl. The dissolution times are 3 ms (2 repeats), 10 ms (12 repeats), 15 ms (12 repeats) and 18 ms (6 repeats).

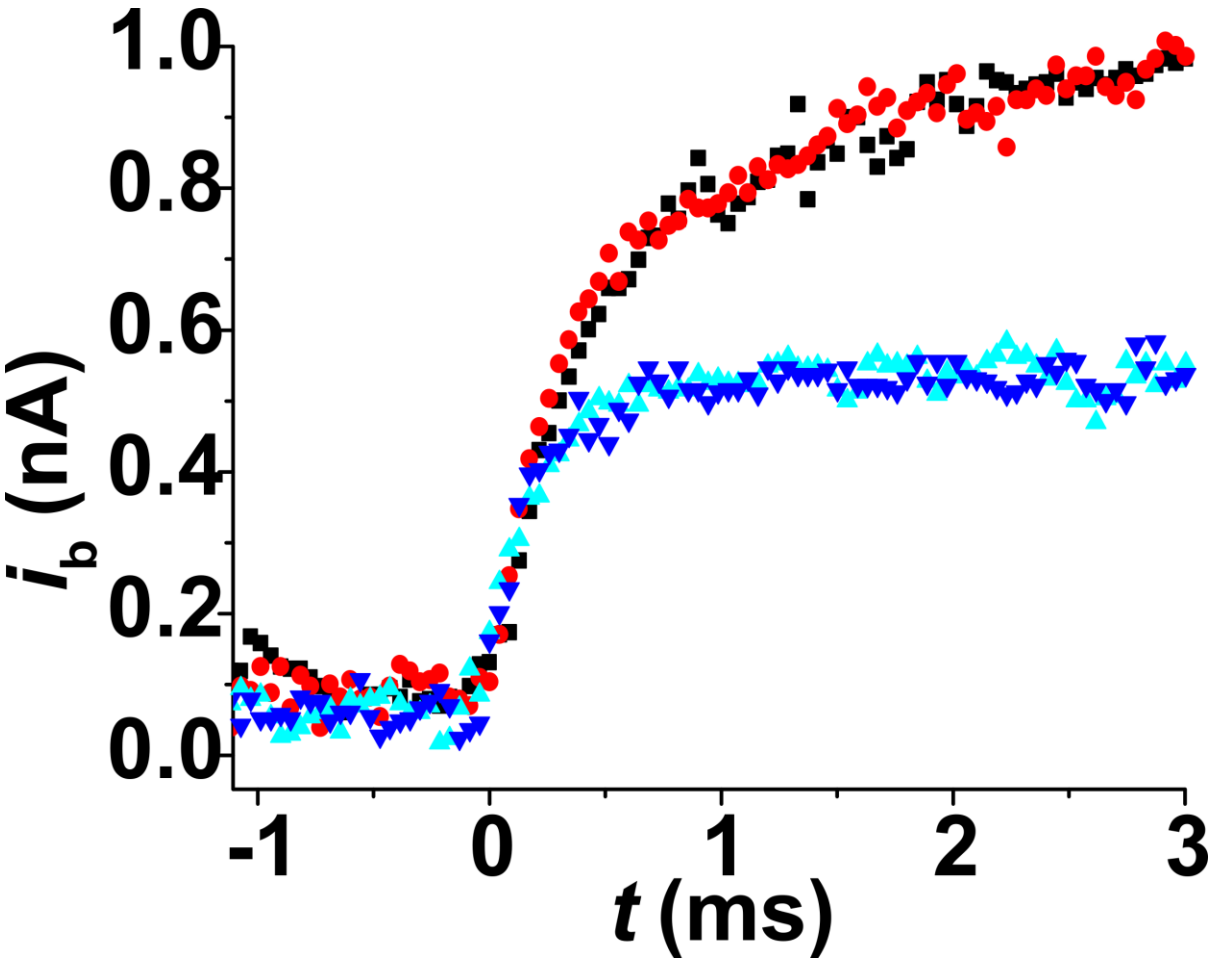

Figure 4. Conductance current-time plot of the meniscus landing on SiO_2 for two runs (▲ and ▼) and two for NaCl (● and ■). Time t = 0 s is defined as the time when the meniscus lands on the surface of the crystal.

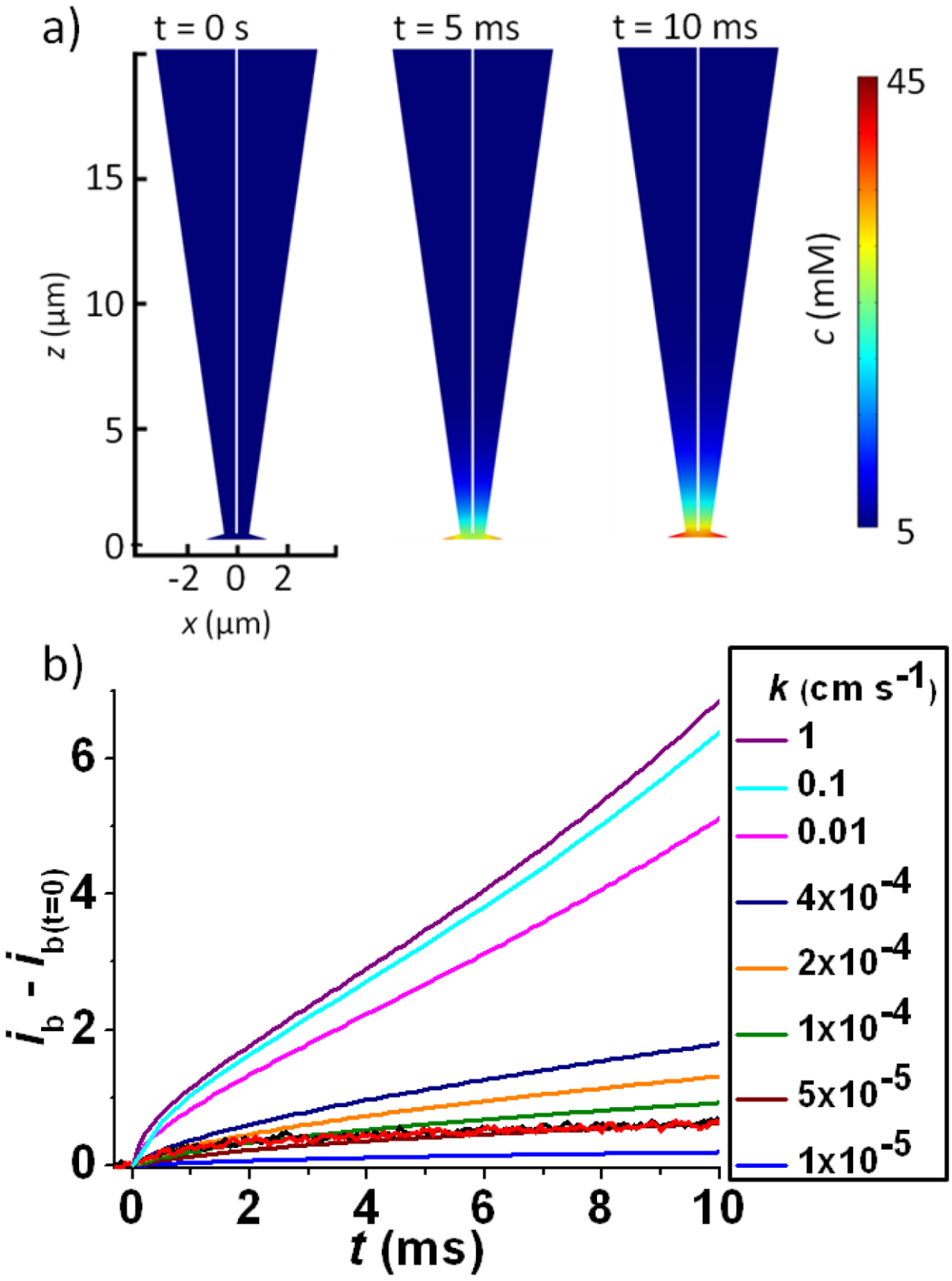

Figure 5. (a) FEM model results showing the concentration of NaCl within a dual-barrel conductance micropipet at time steps: 0 s, 5 ms and 10 ms for a tip of dimensions: m_h = 300

nm, r_p = 0.65 µm, r_t = 0.4 µm, θ = 8°, t_w = 50 nm and m_c = 3.2 µm with k = 5x10^{-5} cm s^{-1}. (b) Simulated conductance current-time plots for a pipet of identical dimensions as (a) on a NaCl substrate with a range of k values. For comparison, 2 sets of typical experimental data are shown (red and black) matching k = 1 x 10^{-4} cm s^{-1} at < 3 ms and k = 5 x 10^{-5} cm s^{-1}.

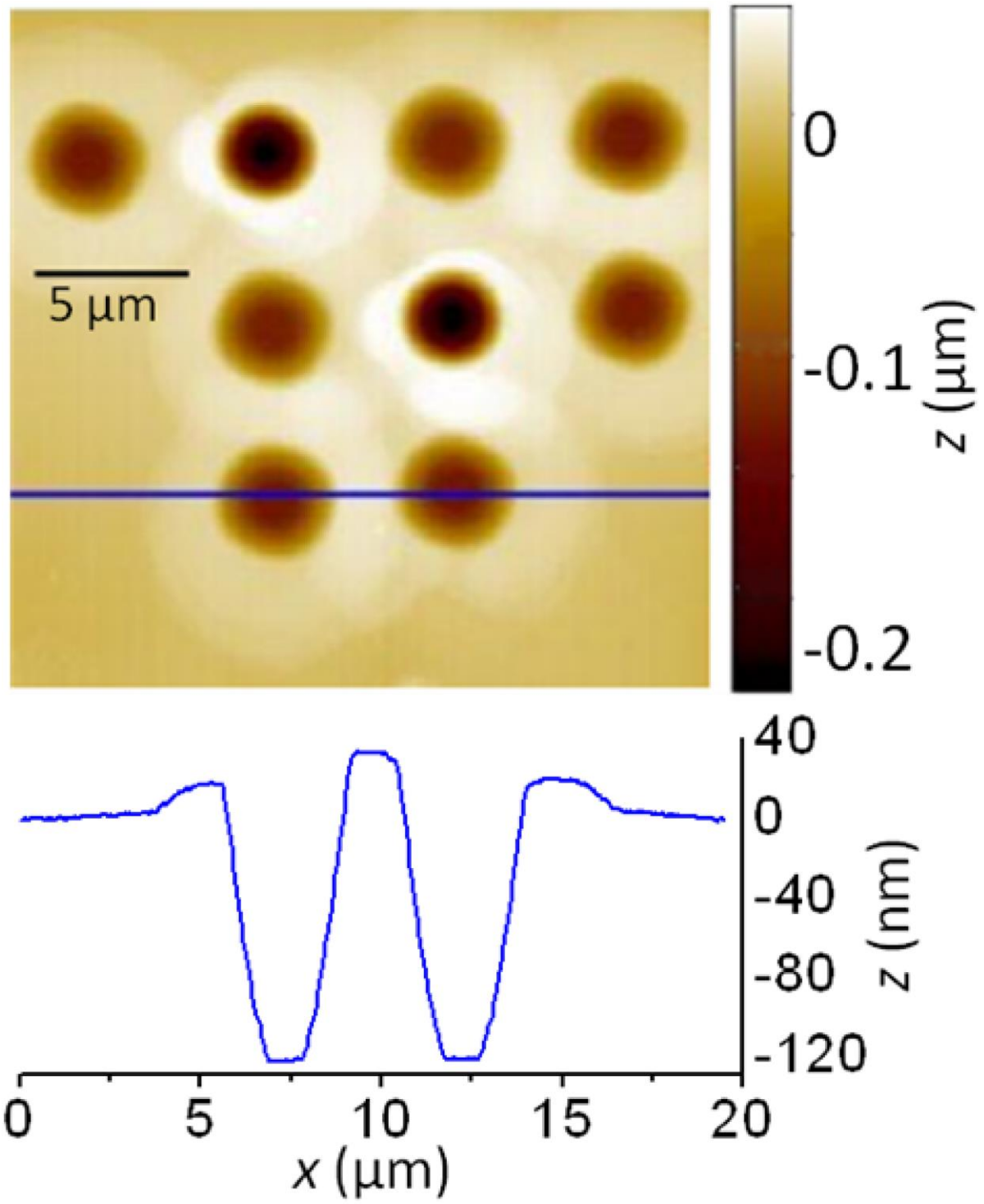

Figure 6. AFM image of typical dissolution pits on a NaCl microcrystal for a contact time of 10 ms. The profile is across the area marked by the blue line.

Table of contents only